https://doi.org/10.1590/jatm.v16.1339 ORIGINAL PAPER

Constraint Control System Design for Double-Body Aircraft and Implementation on a Simulation Platform

Amir Azizi[1*], Yosef Abbasi[1], Seyed Hossein Sadati[1]

1. Malek Ashtar University of Technologies – Department of Aerospace – Tehran – Iran.

*Correspondence author: amirazizi212@gmail.com

ABSTRACT

In this paper, the modeling, open-loop analysis, and design of the constraint control system of the double-body aircraft are discussed. In a double-body aircraft configuration, two identical aircraft are connected using a one degree-of-freedom (1DOF) joint about the longitudinal body axis (hinges at the wingtips). Due to the long-term flight of the aircraft at high lift coefficients and the very high aspect ratio (AR) of the aircraft, controlling the angle of attack and the yaw rate is crucial to staying within safety limits. Additionally, the constraint control algorithm must be implementable in microprocessors to minimize weight and energy consumption. In the present research, a centralized control system with a sliding mode command governor (SMCG) is proposed to address these issues. First, the double-body aircraft was modeled using the Newton-Euler method. A nominal control system was designed with a linear control law, and then a SMCG is presented. To validate the constraint control system, numerical simulation and experimental testing were performed using a double-body simulation platform. The simulation and experimental test results indicate that the proposed control system performs well, with no deviation of the desired states from the limitations accrued.

Keywords: Double-body aircraft; Constraint control; Sliding mode command governor; Modeling.

INTRODUCTION

Nowadays, the ability of unmanned aircraft to fly for extended periods at high altitudes is one of the most important goals of research projects worldwide. High-altitude pseudo satellites (HAPS) fly at low speeds at high altitudes and are used in various applications at a much lower cost than space satellites. Many researches has been carried out in different parts of the world about HAPS aircraft, the most famous of which is the Zephyr drone. To achieve an aircraft with the desired performance, the energy balance and the mass balance of the aircraft must be maintained simultaneously. These parameters result in an aircraft with a high aspect ratio (AR) and elastic wing, which makes the construction of the aircraft very difficult and its flight control complicated. A multi-body configuration can address some of these issues. In this idea, instead of making one big aircraft, several small identical aircraft are connected using 1 or 2 degrees-of-freedom (DOF) joints. In a multi-body configuration, a wing with a very high AR is made up of several sections with a lower AR and has a more convenient manufacturing and assembly process. In addition to the performance requirements for multi-body aircraft flight control systems, certain flight parameters should not deviate from the safety limits. Due to the long-term flight of these aircraft at high lift coefficient, the control of the airspeed and angle of attack must be precise to prevent the aircraft from stalling. In addition, due to the very high AR of the aircraft, the yaw rate will be limited. Because the outer wing sections are reached stall or maximum speed. Aircraft in this configuration introduce forces and moments

Received: Jan 24 2024 | **Accepted:** May 29 2024
Section editor: Alison Moraes
Peer Review History: Single Blind Peer Review.

to each other. The joint mechanism between the aircraft and the connection point to the wing structure are among the sensitive points where the amount of stress should not exceed the tolerance limit. Minimizing the volume, weight and energy consumption of the systems used in this aircraft adds another requirement to minimize the computational load of the flight control algorithm.

The dynamic behavior of coupled aircraft was studied by Magill (2012). The focus of the work has been on the stability analysis based on the model obtained from the results of the wind tunnel tests and the *computational fluid dynamics* (CFD) studies. The aerodynamic interaction of two coupled wings is investigated in Behrens *et al.* (2020). In this study, the induced forces and moments of two identical wings have been investigated numerically and experimentally. The configuration of is proposed in Montalvo and Mark (2015), which is a set of aircraft with different shapes of connections to each other and forming a multi-body aircraft. In this study, the dynamic behavior of the multi-body aircraft has been investigated and dynamic modes change based on how many aircraft are linked together. The controllability of the meta aircraft configuration is studied in Troub and Montalvo (2016). Next, the PID controller with gain scheduling is used for flight control of the compound aircraft. In Köthe and Luckner (2017), modeling and flight path control of a multi-body aircraft is discussed. The multi-body aircraft consisting of 10 smaller aircraft that are connected with 2DOF joints. After open-loop linear analysis, various control loops are designed using H_∞ robust control laws. The rank of the controller reaches 191 in some loops, and after rank reduction, the controller has reached the rank of 61. This issue will practically make its hardware implementation difficult. In other research, the same authors tried to experimentally prove the results of Köthe and Luckner (2017) in Köthe *et al.* (2017). The multi-body aircraft consists of three identical ones, designed and built. The flight control algorithm of the previous work has been designed and implemented for flight tests. The processor of the central processing module must be powerful enough to be able to execute all the control and navigation loops in real time. Unfortunately, in this study, the research team could not conduct a successful flight test due to implementation problems. In line with NASA's Link project, a study has been conducted to connect and couple two aircraft during flight (Cooper and Rothhaar 2018). Two aircraft approach each other at a certain height and perform the connection operation, and then the compound aircraft continues to fly. The authors have used a cascade flight control algorithm with PID control law. The controller coefficients are designed according to the flight phases before and after the connection. The idea of using a multi-body aircraft configuration to increase solar energy production has been proposed in Wu *et al.* (2019). Of course, this idea was mentioned earlier in Odysseus's aircraft. The shape of the wing composed of three smaller aircraft is changed in such a way that the maximum solar energy is acquired. In this study, the flight control of the aircraft is not discussed. The study of the dynamic behavior of multi-body aircraft has also been done in Chao *et al.* (2019). Modeling has been obtained using the estimation of aerodynamic coefficients using the lift line method and Newton-Euler method. Finally, a double-body aircraft consisting of two identical aircraft has been experimentally tested. In Meng *et al.* (2022), the modeling and design of the PID controller for a double-body aircraft has been done, which has had a successful implementation and flight test. In Zhu *et al.* (2023), the modal analysis of a three-body aircraft was discussed and the simulation results of the extracted model were in good agreement with the flight test results. In Cobar and Montalvo (2021), the successful takeoff and landing of a wing-tip-connected meta aircraft prototype has been done. The flight controller on board each aircraft was a Raspberry Pi 3B complete with Navio2 flight controller. The pilot commands both aircraft and each flight controller responds independently to these inputs. The method used in the article cannot be used in an aircraft with more bodies. Also, the relative roll of the two bodies, which must be 0 due to the performance reasons of the aircraft, never approaches 0.

Predictive control law and its derivatives are the best methods for applying constraints in the control systems. However, the high computational load is one of the important reasons for not widely using this method in aerial applications. Especially in applications where processors must be small and have low energy consumption. The use of add-on constraint enforcement systems are more commonly used in aerospace applications. Usually, the nominal control system for the aircraft is already designed in detail, and only the constraint enforcement system is added to it. Add-on constraint control methods have generally been investigated in two forms: reference/command governor and barrier functions (CBF). The reference governor is designed as a low-pass filter function (Ardalan *et al.* 2006), and the filter parameters can be optimally obtained based on the desired cost function (Elmer and Kolmanovsky 1999).

Wei *et al.* (2021) studied the constrained control of a hypersonic aircraft using a backstepping control law with a constrained steering filter. The scramjet engine of the hypersonic aircraft is very sensitive to the angle of attack of the aircraft, and if the angle of attack deviates from the allowed range, can cause thermal suffocation. Similar work has been done for F16/MATV fighter constraint flight control (Lars *et al.* 2007). Zhou *et al.* (2020) studied the constrained control of the path following control for automatic landing using the CBF. The backstepping control law is used for the nominal controller, and CBF formulation was developed to ensure flight path constraint satisfaction. The blocking function is formulated and becomes a *quadratic programming* (QP) problem. Khan *et al.* (2020) have studied the constrained control of a quadrotor. The limitation issue is to limit the flight profile with a safe virtual fence. The basic controller is of non-linear type and is designed as cascade loops. In this research, CBF has been performed as two upstream and downstream functions. The solution method is QP and the numerical simulation shows the success of the design of barrier functions in keeping the aircraft inside the safety fence. Xu *et al.* (2018) have studied the constrained control of the quadrotor using the supervisory blocking function. The system is designed as a teleoperator and all the calculations related to the blocking function are performed on the ground part, and its output is sent to the autopilot of the plane using a telemetry unit. The autopilot of the aircraft uses a Crazyflie2 and a proportional-integral-derivative (PID) controller. In Babaei and Hossein (2021), constraint enforcement using pseudospectral optimization. This method is able to produce a solution satisfying all hard constraints by transforming the optimal control problem into a parametric optimization one. In Prado and Santos (2017), the problem of safely controlling the position trajectory of a multirotor aerial vehicle subjected to a conic constraint on the total thrust vector and a linear convex constraint on the position vector is solved using a linear state-space model predictive control strategy.

In this paper, a constraint flight control system for a double-body aircraft is presented. The goal is to design a control system that reduces costs and performs well against the non-linear behavior of the aircraft and safety limitations. The innovations of this research can be categorized into three parts.

- Centralized control system – In various references, the system architecture is designed based on the distributed flight control system. The proposed control system is centralized and greatly reduces system costs. In the centralized control system, in contrast to the distributed system, there is no need for independent navigation system for the bodies, and rotational measurement sensors are used to measure the angle between them. This architecture solves the problem of attitude estimation error in the navigation system of each body.
- Sliding mode command governor (SMCG) – An add-on constraint control system based on sliding mode has been designed to prevent deviations of certain states from the safety restrictions. This system is very simple and robust and does not require accurate modeling of the aircraft. Unlike the optimization-based methods, the computational load of this add-on system is so low that it can be implemented in small processors.
- Implementation and experimental testing – The double-body experimental testing platform helps a lot to understand the dynamics of multi-body systems. The evaluation of the constraint control system has been done using the hardware implementation in the test platform.

In the next parts of the article, the modeling and analysis of the double-body aircraft will be discussed first. Then, in the following, the designs of the nominal flight control system and add-on constraint control are presented. In the fourth part, the numerical simulation results are discussed. The fifth section brought up the implementation and experimental testing results. At the end, conclusions and suggestions for further research will be presented.

Flight dynamics and analysis

Single aircraft

As presented in the introduction, the double-body aircraft consists of two identical aircraft that are connected using a hinge mechanism. The hinge mechanism allows the two aircraft to have rotational freedom about each other around the longitudinal axis. In this section, firstly, the modeling and analysis of a typical aircraft used in a multi-body configuration is presented (Table 1).

Table 1. Aircraft specifications.

Parameter	Value
Total mass	20 Kg
Wing area	1.45 m^2
Wingspan	4.82 m
Mean aerodynamic chord	0.307 m
Cruise speed	25 m·s

Source: Elaborated by the authors.

This aircraft has an electric propeller motor, ailerons, elevator, and rudder. The modeling of the aircraft is done with the assumption of being rigid, and the 6DOF equations of motion are written as follows (Zipfel 2000).

$$m\mathrm{D}^{\mathrm{M}}\mathbf{v}_{\mathbf{M}}^{\mathbf{I}} = \mathbf{F}_{\mathbf{M}} + m\mathbf{g} - m\boldsymbol{\Omega}^{\mathbf{MI}}\mathbf{v}_{\mathbf{M}}^{\mathbf{I}} \tag{1}$$

$$\mathbf{I}_{\mathbf{M}}^{\mathbf{M}}\mathrm{D}^{\mathrm{M}}\boldsymbol{\omega}^{\mathbf{MI}} = \mathbf{M}_{\mathbf{M}} - \boldsymbol{\Omega}^{\mathbf{MI}}\mathbf{I}_{\mathbf{M}}^{\mathbf{M}}\boldsymbol{\Omega}^{\mathbf{MI}} \tag{2}$$

where in Eqs. 1 and 2 $m\mathrm{D}^{\mathrm{M}}\mathbf{v}_{\mathbf{M}}^{\mathbf{I}}$ and $\mathrm{D}^{\mathrm{M}}\boldsymbol{\omega}^{\mathbf{MI}}$ are the rotational time derivative of the aircraft linear and angular speed with respect to body frame (M), $\mathbf{F}_{\mathbf{M}}$ is the result of the aerodynamic force and the thrust on the aircraft, and $\mathbf{M}_{\mathbf{M}}$ is the torques on the aircraft, which are all can be written in the body coordinate system. Also, $\boldsymbol{\Omega}^{\mathbf{MI}}$ is the skew-symmetric matrix of the $\boldsymbol{\omega}^{\mathbf{MI}}$ vector.

The $\mathbf{F}_{\mathbf{M}}$ and $\mathbf{M}_{\mathbf{M}}$ has formulation as:

$$\left[\mathbf{F}_{\mathbf{M}}\right]^{\mathrm{M}} = \begin{bmatrix} \bar{q}SC_X + T \\ \bar{q}SC_Y \\ \bar{q}SC_Z \end{bmatrix} \tag{3}$$

$$\left[\mathbf{M}_{\mathbf{M}}\right]^{\mathrm{M}} = \begin{bmatrix} \bar{q}SbC_l \\ \bar{q}S\bar{c}C_m \\ \bar{q}SbC_n \end{bmatrix} \tag{4}$$

$$\begin{Bmatrix} C_L \\ C_D \\ C_y \end{Bmatrix} = \begin{Bmatrix} C_{L0} + C_{L\alpha}\alpha + C_{Lq}\dfrac{q\bar{c}}{2V_T} + C_{L\delta_e}\delta_e \\ C_{D0} + C_{D\alpha}\alpha + C_{D\delta_e}|\delta_e| \\ C_{y\beta}\beta + C_{yp}\dfrac{pb}{2V_T} + C_{yr}\dfrac{rb}{2V_T} + C_{y\delta_a}\delta_a + C_{y\delta_r}\delta_r \end{Bmatrix} \tag{5}$$

$$\begin{Bmatrix} C_l \\ C_m \\ C_n \end{Bmatrix} = \begin{Bmatrix} C_{l\beta}\beta + C_{lp}\dfrac{pb}{2V_T} + C_{lr}\dfrac{rb}{2V_T} + C_{l\delta_a}\delta_a + C_{l\delta_r}\delta_r \\ C_{m0} + C_{m\alpha}\alpha + C_{mq}\dfrac{q\bar{c}}{2V_T} + C_{m\delta_e}\delta_e \\ C_{n\beta}\beta + C_{np}\dfrac{pb}{2V_T} + C_{nr}\dfrac{rb}{2V_T} + C_{n\delta_a}\delta_a + C_{n\delta_r}\delta_r \end{Bmatrix} \tag{6}$$

where in Eqs. 3-6, $q\bar{c}$ is the dynamic pressure, S is wing area of the aircraft, b is the wingspan, and T is the thrust. The values of the aerodynamic coefficients of the aircraft are shown in Table 2.

Table 2. Aerodynamic coefficients of the aircraft.

C_{L0}	$C_{L\alpha}$	C_{Lq}	$C_{L\delta_e}$	C_{D0}	$C_{D\alpha}$	$C_{D\delta_e}$	$C_{y\beta}$	C_{yp}	C_{yr}	$C_{y\delta_a}$	$C_{y\delta_r}$	C_{nr}
0.23	0.09	4.62	0.0065	0.37	0.0018	0.0034	-0.006	-0.04	1.74	0.025	-0.23	-0.28
C_{m0}	$C_{m\alpha}$	C_{mq}	$C_{m\delta_e}$	$C_{l\beta}$	C_{lp}	C_{lr}	$C_{l\beta_a}$	$C_{l\delta_r}$	$C_{n\beta}$	C_{np}	$C_{n\delta_a}$	$C_{n\delta_r}$
0.001	-0.018	-5.52	-0.02	-0.001	-0.72	0.104	0.29	0.008	0.001	-0.12	0.004	-0.053

Source: Elaborated by the authors.

Linearization and decoupling of the state variables at the equilibrium point V = 25 m·s and H = 8,000 m were performed for the aircraft and the trim angle of attack was 6.37 degrees, the thrust force was 8.5 N, and the trim elevator angle was -5.67 degrees. The aircraft has two longitudinal dynamic modes, phugoid and short period, which are oscillating and stable, and in the lateral-directional channels, a stable spiral mode with a large time constant, a stable oscillating Dutch roll mode, and a stable toll mode with a small time constant were obtained (Table 3).

Table 3. Eigenvalues analysis results of single aircraft.

No.	Mode	Eigenvalues	Damping	Frequency (rad/s)	State
1	Roll	-14.67	1	14.67	Stable
2	Spiral	-0.005	1	0.005	Stable
3	Dutch roll	-1.88 ± 2.36i	0.62	3.01	Stable
4	Short period	-1.64 ± 4.06i	0.37	4.38	Stable
5	Phugoid	-0.0037 ± 0.53i	0.006	0.53	Stable

Source: Elaborated by the authors.

Double-body aircraft

Newton-Euler method, Lagrange method, and Kane's method are three approaches often used in multi-body dynamics (Meng Y *et al.* 2022). In this paper, Newton-Euler method is used because of the simplicity and intuitiveness. The equations of motion for clusters of bodies (Zipfel 2000) can be written as:

$$\sum_k D^I(\mathbf{I}_{B_k}^{B_k}\boldsymbol{\omega}^{B_kI}) + \sum_k m^k \mathbf{S}_{B_kC} D^I D^I \mathbf{s}_{B_kC} = \sum_k \mathbf{M}_k + \sum_k \mathbf{S}_{B_kC}\mathbf{F}_k \tag{7}$$

$$D^I D^I \mathbf{s}_{CI} = \sum_k \frac{\mathbf{F}_k}{m^k} \tag{8}$$

where in Eqs. 7 and 8, m^k is the mass of kth aircraft, $\mathbf{S}_{B_kC}$ is the displacement vector of kth aircraft center of mass (CM) from common CM, $\mathbf{S}_{B_kC}$ is the skew-symmetric matrix of $\mathbf{S}_{B_kC}$, $\mathbf{M}_k$ is moment vector acting on kth aircraft, and $\mathbf{F}_k$ is the result of aerodynamic, gravity, and thrust forces of each aircraft.

To determine the individual displacement vectors ($\mathbf{S}_{B_kC}$), geometrical equations may be used as:

$$\begin{cases} \sum_k m^k \mathbf{s}_{B_kC} = 0 & k = 1,2,\ldots \\ \mathbf{s}_{B_1C} - \mathbf{s}_{B_jC} = -\mathbf{s}_{B_jB_1} & j = 2,3,\ldots \\ \mathbf{s}_{B_kI} - \mathbf{s}_{B_kC} = \mathbf{s}_{CI} & k = 1,2,\ldots \end{cases} \tag{9}$$

Figure 1 shows the graphical concept of the double-body aircraft and their body frame. This aircraft consists of two identical aircraft that are connected by one degree-of-freedom (1DOF) joint around the body axis 1 at the wingtips. The main and the left aircraft are named M and P in that order. Modeling is done based on the centralized control system and the use of rotational measurement sensors at the hinge location.

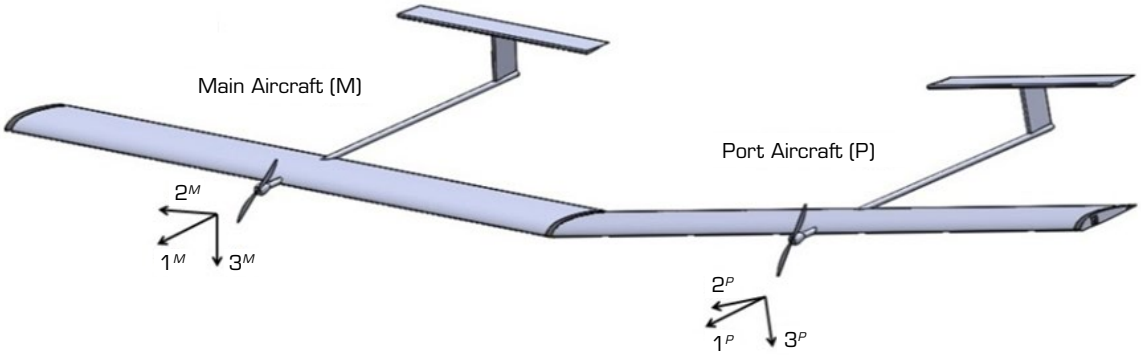

Source: Elaborated by the authors.

Figure 1. Graphical concept of the double-body aircraft.

The displacement vector s is expressed in the main aircraft body coordinate system, and Φ is the angle between the two wings of the aircraft. Therefore, the geometric relationships of the relative position and angle of two aircraft in the body coordinate system M are written as follows:

$$\left[\mathbf{s_{PM}}\right]^{\mathrm{M}} = \begin{bmatrix} 0 \\ -\frac{b}{2} - \frac{b}{2}\cos\Phi \\ -\frac{b}{2}\sin\Phi \end{bmatrix} \tag{10}$$

$$\left[\boldsymbol{\omega}^{\mathbf{PM}}\right]^{\mathrm{M}} = \begin{bmatrix} \dot{\Phi} \\ 0 \\ 0 \end{bmatrix} \tag{11}$$

$$\left[\mathrm{D}^{\mathrm{M}}\boldsymbol{\omega}^{\mathbf{PM}}\right]^{\mathrm{M}} = \begin{bmatrix} \ddot{\Phi} \\ 0 \\ 0 \end{bmatrix} \tag{12}$$

Now the 7DOF equations of motion in main aircraft coordinate system can be written as:

$$\mathrm{m}\left[\mathrm{D}^{\mathrm{M}}\mathbf{v}_{\mathbf{M}}^{\mathbf{I}}\right]^{\mathrm{M}} = \left[\mathbf{F}_{\mathbf{M}\mathfrak{l}}\right]^{\mathrm{M}} + \mathrm{m}\left[\mathbf{g}\right]^{\mathrm{M}} - \mathrm{m}\left[\boldsymbol{\Omega}^{\mathbf{MI}}\right]^{\mathrm{M}}\left[\mathbf{v}_{\mathbf{M}}^{\mathbf{I}}\right]^{\mathrm{M}} \tag{13}$$

$$\left[\mathbf{I}_{\mathbf{M}}^{\mathbf{M}}\right]^{\mathrm{M}}\left[\mathrm{D}^{\mathrm{M}}\boldsymbol{\omega}^{\mathbf{MI}}\right]^{\mathrm{M}}=\left[\mathbf{M}_{\mathbf{Mt}}\right]^{\mathrm{M}}-\left[\boldsymbol{\Omega}^{\mathbf{MI}}\right]^{\mathrm{M}}\left[\mathbf{I}_{\mathbf{M}}^{\mathbf{M}}\right]^{\mathrm{M}}\left[\boldsymbol{\Omega}^{\mathbf{MI}}\right]^{\mathrm{M}} \tag{14}$$

$$\left[\mathrm{D}^{\mathrm{M}}\boldsymbol{\omega}^{\mathbf{PM}}\right]^{\mathrm{M}}=f\left(\mathbf{F}_{\mathbf{M}},\mathbf{F}_{\mathbf{P}},\mathbf{M}_{\mathbf{M}},\mathbf{M}_{\mathbf{P}},\dot{\Phi},\Phi\right) \tag{15}$$

where $\mathbf{F}_{\mathbf{Mt}}$ and $\mathbf{M}_{\mathbf{Mt}}$ are the total forces and moments acting on the main aircraft. In the 7DOF equations of motion expressed in Eqs. 13-15, the input vector is u = [δ_{ailM}, δ_{elM}, δ_{ruM},δ_{thM}, δ_{ailP}, δ_{elP}, δ_{ruP}, δ_{thP}]^T. For stability analysis, the double-body aircraft model is linearized at the equilibrium point of V = 25 m·s, H = 8,000 m, and a relative roll angle of 0 degree. The angle of attack of the trim of both aircraft is 6.26 degrees, the thrust force of each engine is 8.45 N, and the trim elevator of each is equal to -5.57 degrees. For the M aircraft, the trim aileron is equal to -1.31 degrees. Trim aileron for the aircraft P is the same value and positive. As expected, the trim conditions of double-body and single aircraft are significantly different. Thrust, elevator, and trim angle of attack are reduced due to the increase in configuration performance, and the lateral-directional trim has non-zero values due to the asymmetry of pressure distribution on each wing. Seven different modes with different root locations were identified for the double-body aircraft (Table 4). Using linear system stimulation in the direction of eigenvectors related to each mode, the types and properties of the modes could be identified.

Table 4. Eigenvalues analysis results of double-body aircraft.

No.	Mode	Eigenvalues	Damping	Frequency (rad/s)	State
1	Roll	-15.6	1	15.6	Stable
2	Spiral	-0.067	1	0.067	Stable
3	Dutch roll	-0.24 ± 0.66i	0.34	0.7	Stable
4	Short period	-1.61 ± 3.98i	0.37	4.3	Stable
5	Phugoid	-0.004 ± 0.53i	0.007	0.53	Stable
6	Relative roll i	-5.16	1	5.16	Stable
7	Relative roll ii	0.066	-1	0.066	Unstable

Source: Elaborated by the authors.

By comparing the eigenvalues of the double-body with the single aircraft (Tables 3 and 4), it can be seen that the locations of the roots of the longitudinal modes do not change much, with major changes occurring in the lateral-directional modes. This issue is due to the connection of two aircraft in width. The double-body aircraft has a higher AR and its lateral-directional dynamic behavior will undergo more changes. In the double-body configuration, the roll mode appears with a higher frequency and the Dutch roll mode has a lower frequency and damping. The spiral mode also had a few changes and its frequency has decreased slightly. The important point is the addition of two new modes to the linear system, which are the stable relative roll with high frequency and the unstable relative roll with low frequency. The physical forms of these two modes are shown in Fig. 2.

Control system design

In this section, the architecture of the double-body aircraft flight control system is discussed first. In the following, the design of the nominal control law and then the add-on extension system are examined.

Control system architecture

Systemically, the centralized flight control system differs significantly from the examples cited in references (Chao *et al.* 2019; Köthe and Luckner 2017; Meng *et al.* 2022). In these references, the system architecture is designed based on the existence of a distributed and decentralized flight control system. The proposed control system is centralized and results in a substantial reduction in system costs. In the centralized control system, unlike the distributed system, there is no need for independent navigation systems

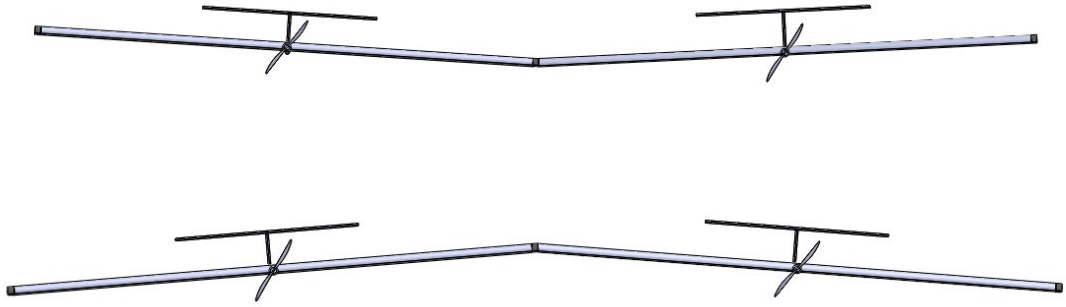

Source: Elaborated by the authors.

Figure 2. Stable relative roll (top) and unstable relative roll (bottom).

for the aircraft, and rotational measurement sensors are used to measure the angle between the aircraft. This method allows the flight control to be designed based on the measurable parameter. The cost reduction in the redundant flight management system (FMS) becomes more evident as there is no requirement for a redundant FMS in all aircraft. Figure 3 shows the schematic of the centralized control system.

The FMS block consists of Global Positioning *System* (GPS)/Inertial Navigation *System* (*INS*)/AirData navigation subsystems, flight guidance and control, and radio communication. All matters related to data acquisition, algorithm processing, and command generation are done in this system. The propulsion system block (PS) includes electronic speed control, motor, and propeller. There are aileron and elevator blocks in both M and P aircraft. The rotary encoder (RE) block is coupled to the hinge between the two aircraft. The signal generation board (SGB) is in the P aircraft and the FMS is in the M aircraft; they communicate with each other using the controller area network (CAN) data bus. The SGB block converts the commands generated by the FMS into proper signals for the servos. The power unit (PU) includes battery packs, regulators, and a solar panel maximum power point tracking (MPPT) board. The path and types of the signals and electrical power are shown in Fig. 3.

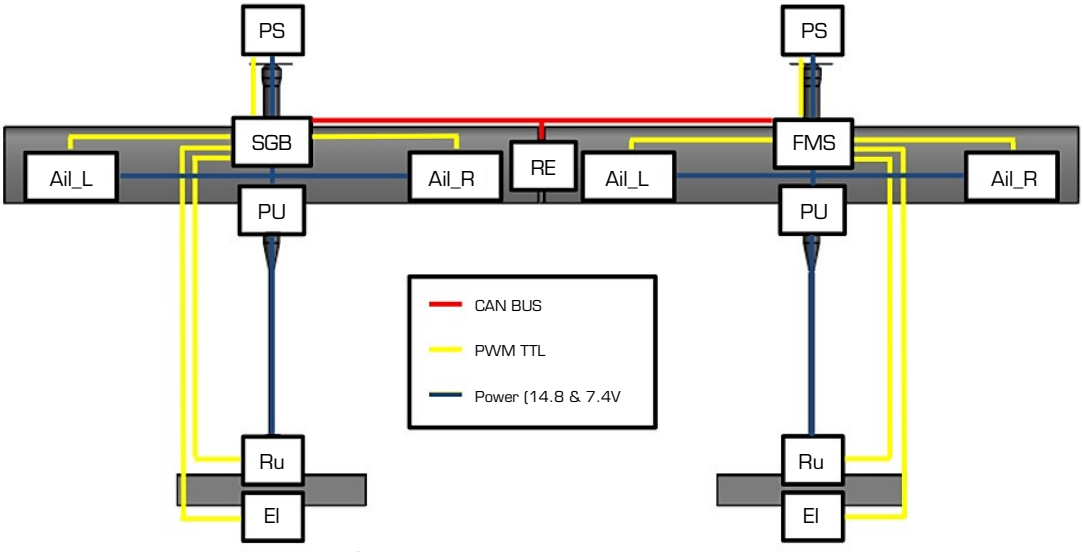

Source: Elaborated by the authors.

Figure 3. Architecture of centralized flight control system.

Nominal flight control law

In the design of the control structure, the main aircraft (M) is based, and if it is assumed that the relative roll angle is kept close to 0, the double-body aircraft behaves like a single larger aircraft. Therefore, in the control assignment of the longitudinal channel, two integrated aircraft elevators can be used jointly. The proposed control structure has three control channels for height, direction, and airspeed (Fig. 4). Altitude and direction control channels have cascaded loops, while the airspeed control channel of the aircraft includes a loop and a classical control law. The output of the height control loop is the steering screw angle and the output of the screw control loop is the deviation of the plane's elevator control surfaces. Lateral control also has side control cascading loops, an M aircraft roll angle, and a relative roll angle regulatory loop. The output of the roll and relative roll control loops are the deviations of the pitch control surfaces of the aircraft. The inner loop controller commands for the main aircraft aileron, elevator, rudder, and port aircraft aileron are shown below:

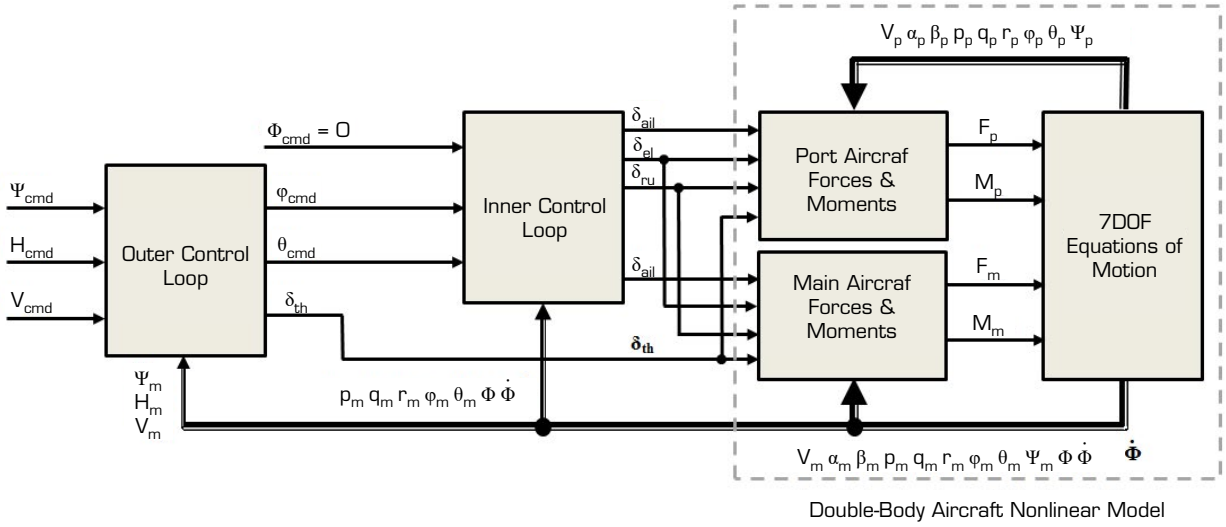

Source: Elaborated by the authors.

Figure 4. Double-body aircraft nominal control block diagram.

$$\begin{aligned}
\delta_{am} &= K_{p_{am}}(\varphi_c - \varphi_m) + K_{i_{am}}\int(\varphi_c - \varphi_m)dt \\
\delta_e &= K_{p_e}(\theta_c - \theta_m) + K_{i_e}\int(\theta_c - \theta_m)dt \\
\delta_r &= -K_{p_r} r_m \\
\delta_{ap} &= -K_{p_{ap}}\varphi_p - K_{i_{ap}}\int\varphi_p dt
\end{aligned} \tag{16}$$

The velocity and outer loop control laws are written as:

$$\begin{aligned}
\varphi_c &= K_{p_\varphi}(\psi_c - \psi_m) \\
\theta_c &= K_{p_\theta}(H_c - H_m) \\
\delta_T &= K_{p_T}(V_c - V_m) + K_{i_T}\int(V_c - V_m)dt
\end{aligned} \tag{17}$$

A settling time of less than 1.5 seconds for the internal fast loop, a settling time of less than 25 seconds, and an overshoot of less than 20% for the external loops are considered to select the gains of the controllers (Table 5).

Table 5. Gains of the nominal control loops.

Control loop	Gains
Speed	$K_p = 5$, $K_i = 0.5$
Pitch	$K_p = -0.522$, $K_i = -0.065$
Height	$K_p = 0.5$, $K_i = 0.05$
Roll and relative roll	$K_p = 1.7$, $K_i = 0.7$
Heading	$K_p = 0.35$

Source: Elaborated by the authors.

SMCG

As mentioned earlier, in addition to the performance requirements for multi-body aircraft flight control systems, some flight parameters like the angle of attack and yaw rate should not deviate from the safety limits. The simplest solution to constraint add-on control is to use a command filter. The command filters can apply constraints in the control system, but the performance of the control system is reduced in general. This is while the system may deviate from the restrictions only in certain conditions. If it is possible to make the command filter so intelligent, it only comes into action in the necessary conditions. In this case, the overall performance of the system will be nominal and the performance will decrease only in the conditions of deviation from the constraints. The SMCG add-on system is a variable bandwidth command filter (Fig. 5). The bandwidth of the filter is controlled by the sliding mode controller in such a way that a specific system state does not exceed the set limits. Unlike other add-on systems, this system does not require a precise model of the system and is highly resistant to parameter changes.

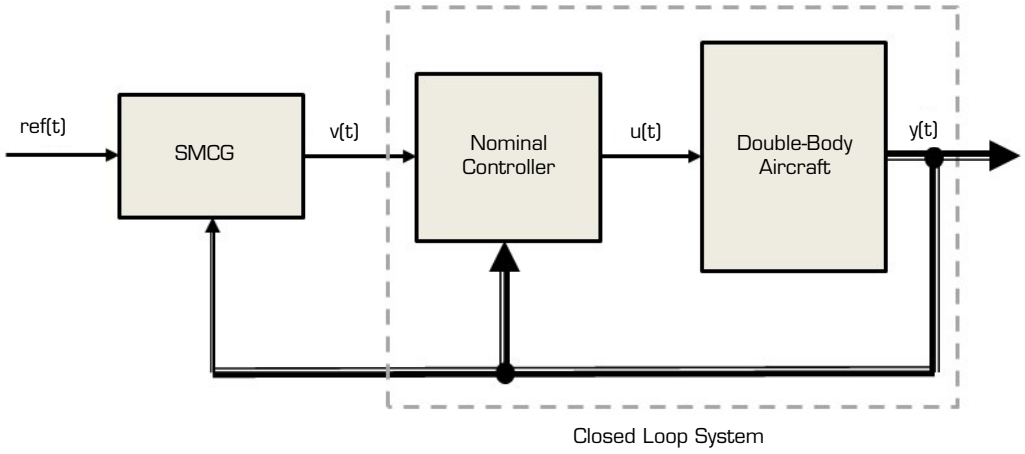

Source: Elaborated by the authors.

Figure 5. SMCG add-on system.

The mathematical model of the filter is as follows:

$$B = \text{sat}_0^S(\dot{e} + Ke) \tag{18}$$

where $B = \text{sat}_0^S(\ )$ is the saturation function with variable range B and this range is determined by sliding mode control. The ref is command input, y is filter output, and ω_n, ζ are the natural frequency and damping of the filter. The sliding mode controller is also modeled as follows using the saturating function.

$$B = \text{sat}_0^S(\dot{e} + Ke) \tag{19}$$

In this equation, e is the difference of the certain state from the specified limit and K and S are also design parameters. Since the SMCG is added as an extension to the nominal control system, in this section only the stability analysis of the add-on system is discussed. Let $\zeta = [(\nu\ \dot{\nu}]^T$ and lyapunov function candidate chosen as $V = 1/2\ \zeta^T$ then it can be written:

$$\dot{V} = \frac{1}{2}(\nu\dot{\nu} + \dot{\nu}\ddot{\nu}) = -2\zeta\omega_n\dot{\nu}^2 < 0 \qquad \text{if} \qquad \zeta\omega_n > 0 \tag{20}$$

Therefore, **V** is the lyapunov function and the closed loop system will have a bounded output for bounded input.

Numerical simulation

In this section, the numerical simulation of the nominal control system and the constrained control system designed for the double-body aircraft is discussed. The control system simulation results are summarized in Figs. 6 and 7. The double-body

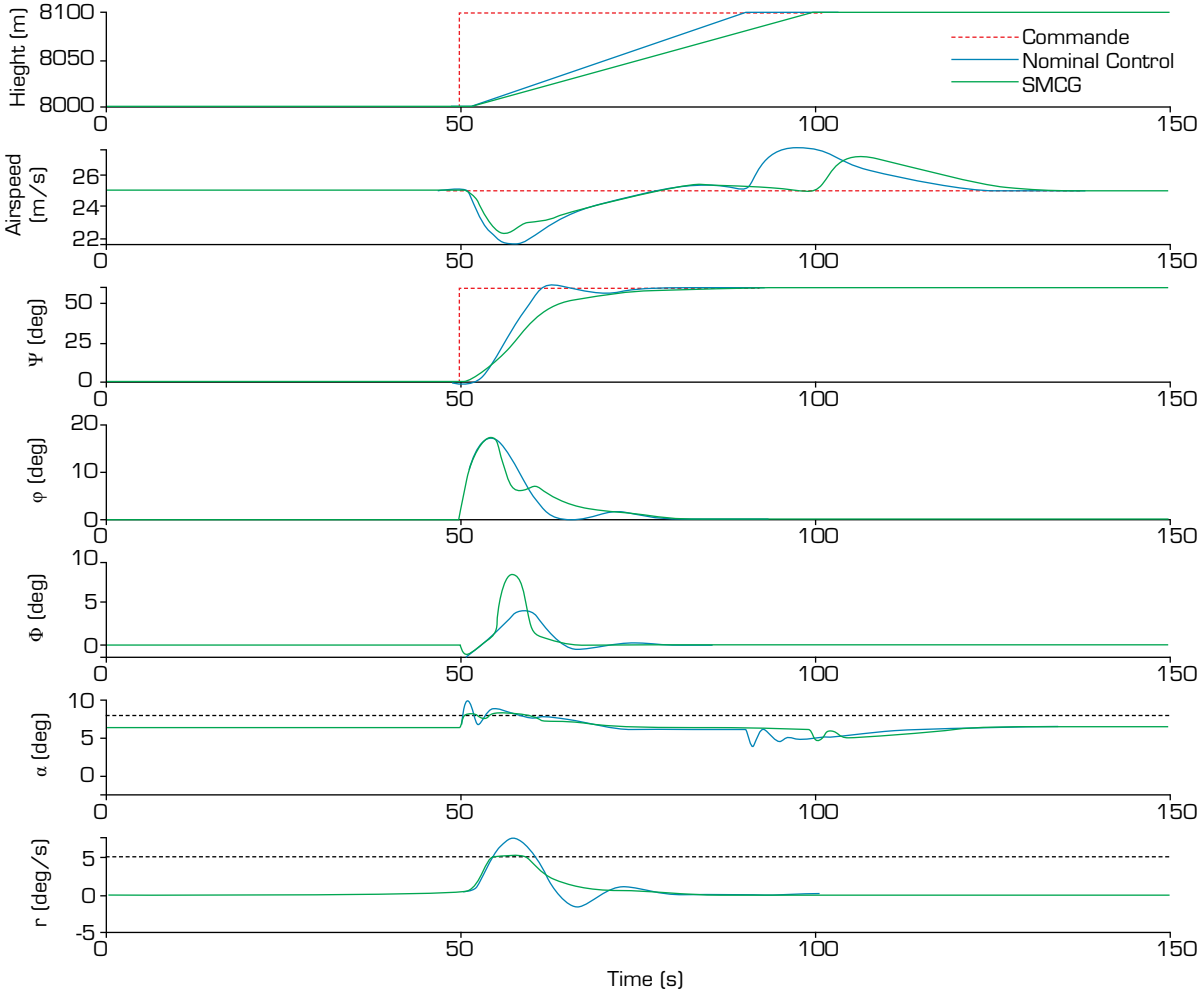

Source: Elaborated by the authors.

Figure 6. Flight parameters change diagram for nominal control system (blue lines) and SMCG bound control system (green lines).

aircraft was flying at an altitude of 8,000 m, with a speed of 25 m per second in trim conditions, and in 50 seconds a heading command of 60 degrees and an altitude command of 8,100 m were applied to it. As seen in Fig. 6 (blue lines), the nominal control system was able to follow the command of 60 degrees at a rate of 1 degree per second, with a climb rate of about 1.15 m per second. The linear speed changes were less than 3 m·s despite the extreme commands. Relative roll changes were limited to less than 5 degrees. The angle of attack and yaw rate have exceeded the safety limits several times. The safety limits for the angle of attack were to -3.8 degrees and the limits for the yaw rate were set to -5.5 degrees per second (black dashed lines). The commands for the deflection angles of the control surfaces and thrusts of both aircraft were limited and reasonable, allowing and common servos to follow them (Fig. 7 [blue lines]). The same flight scenario was repeated for the SMCG constrained flight control system. Figure 6 (green lines) shows the commands and the output values of the control system's outer loops. The control system followed the height and heading commands with less bandwidth than the nominal control system, which is due to the satisfaction of safety limits for the angle of attack and the yaw rate. As can be seen, immediately after crossing the determined limits for the angle of attack and yaw rate, the SMCG system comes into action and changes the commands, so that these parameters remain within the allowed range. Relative roll changes were limited to less than 8 degrees. The changes were much more limited and smooth than the outputs of the nominal control system. The deflection angles of the control surfaces and thrusts of both aircraft are shown in Fig. 7 (green lines), which were limited and reasonable.

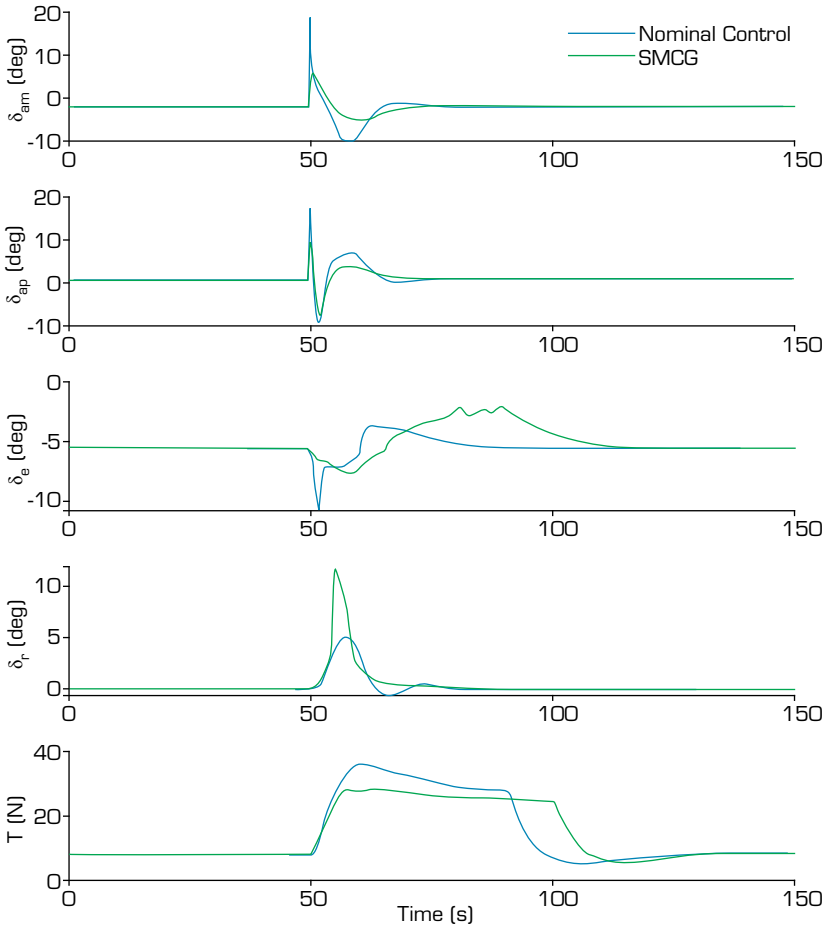

Source: Elaborated by the authors.

Figure 7. Control input change diagram for nominal control system (blue lines) and SMCG bound control system (green lines).

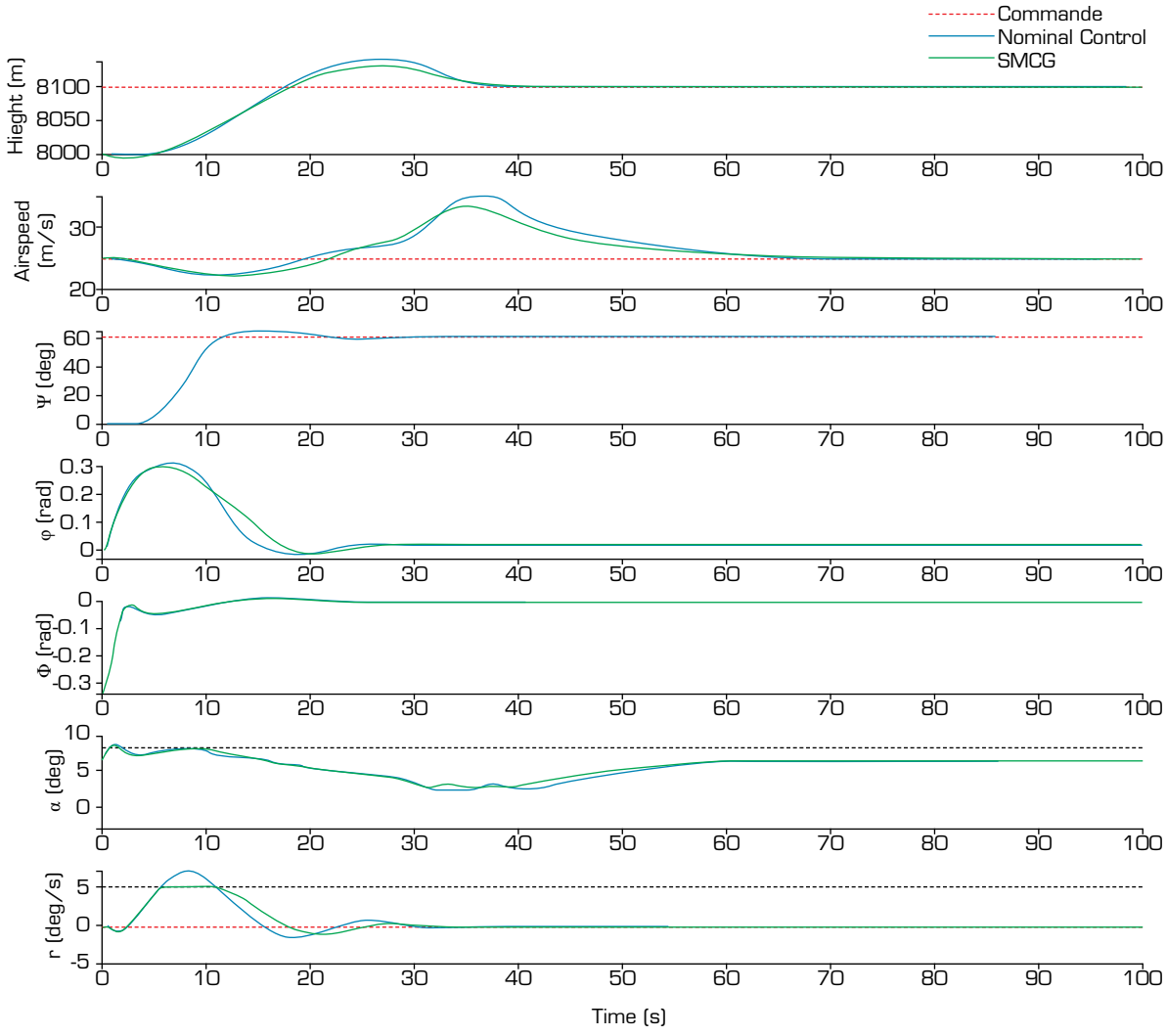

Source: Elaborated by the authors.

Figure 8. Flight parameters change diagram for nominal control system (blue lines) and SMCG bound control system (green lines) in second scenario.

After using SMCG, the control effort increased in some inputs compared to the nominal control and decreased in others. Overall, the changes in control effort were small and are presented for comparison purposes only. Changes in percentage for main aircraft aileron -1.28%, elevator +0.48%, rudder +52%, port aircraft aileron +2.2%, and throttle -0.3% have changed compared to nominal control.

The second simulation scenario represents the worst case. The command inputs are similar to the previous scenario, but it is assumed that the aircraft was affected by disturbances before the inputs were applied. The disturbance caused the relative roll angle to be -20 degrees, which is the worst case. The simulation results are shown in the Figs. 8 and 9. As can be seen, the SMCG has been able to prevent the deviation of the parameters from the safety limits. In this scenario, the changes in control effort (in most cases) are small. Changes in percentage for main aircraft aileron -2.8%, elevator +2.3%, rudder +81%, port aircraft aileron +2.7%, and throttle input -1.4% have changed compared to nominal control.

Experimental test of SMCG control system

To experimentally test the designed control system, a double-body robot platform was designed and built. This platform is suitable for a better understanding of the dynamics of the double-body aircraft and for experimental testing of the control system at

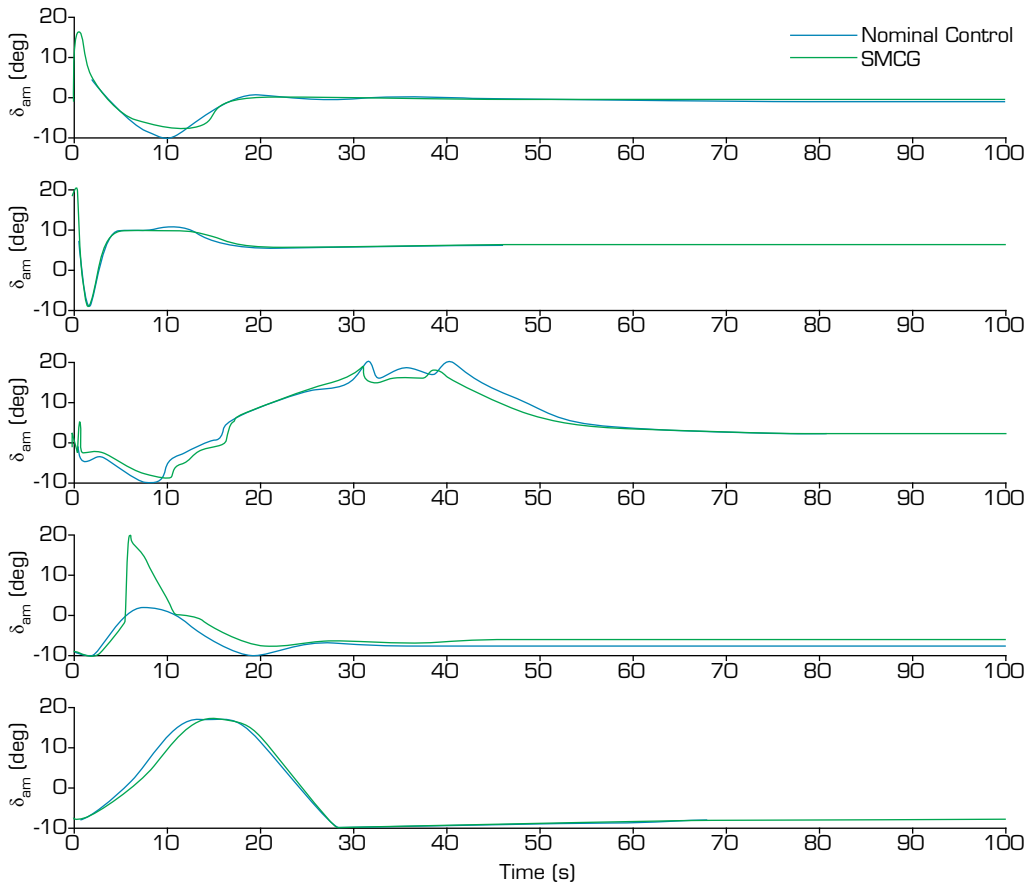

Source: Elaborated by the authors.

Figure 9. Control input change diagram for nominal control system (blue lines) and SMCG bound control system (green lines) in second scenario.

a much lower costs. The platform consists of two identical car robots connected by a 1DOF hinge (Fig. 10). The dynamic behavior of the platform in the forward trim movement mode is similar to the horizontal trim flight of the double-body aircraft. To create more similarity, the inner motors are given 5% more pulse width modulation (PWM) input. This issue simulates the asymmetric lift generated along the wings. The main robot carries a digital signal *processor* (DSP) processor board, inertial measurement unit (IMU), and motor control board. The second robot only has a drive set and receives its commands from the main car's processor. The processor used is the TMS320F2812, which operates at 150 MHz and 150 MIPS and has 128 KWords of internal memory. To measure inertial parameters, a 9DOF IMU model ADIS16405 from Analog Device Company was used. To estimate the heading angle of the main robot, an extended Kalman filter (EKF) is used. The motor drive is an H-bridge model L298. The rotary sensor is also a 10 KΩ potentiometer and the analog output is acquired using the 12-bit analog input of the processor board.

After the implementation and testing of the nominal control system that runs with a frequency of 100 Hz, the results of Fig. 11 have been obtained. The 40-degrees side step command is applied after 4 seconds from the start of the trim movement.

The ψ, Φ, r, and u are respectively the yaw angle, relative roll of the two robots, yaw rate, and control input in as a percentage of PWM. As seen in Fig. 11 (blue lines), the nominal control system has followed the input command, but the yaw rate has exceeded the range of 10 degrees/second several times (black dashed lines). The angle between the two cars is also limited. Figure 11 (green lines) shows the results of the SMCG system. It can be seen that after crossing the limit once due to the low torques of the motors, the SMCG was activated and no crossing of the set limit has occurred. As shown in Fig. 11 (green lines), the bandwidth of the control system is reduced and the settling time for following the command is increased by about 2 seconds.

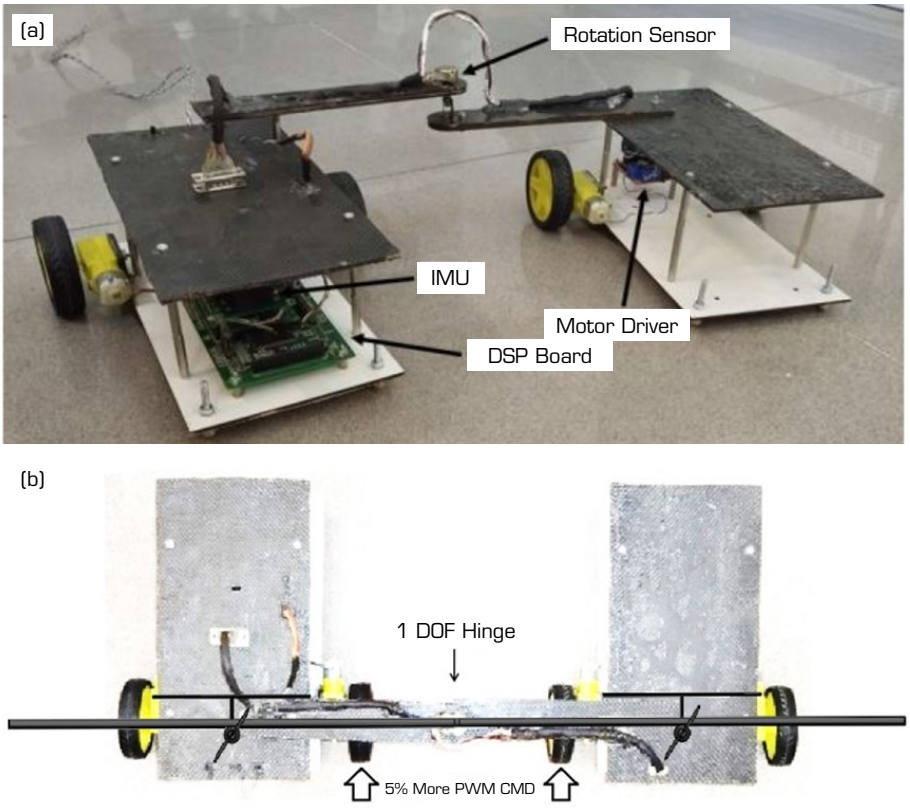

Source: Elaborated by the authors.

Figure 10. The components of the experimental test platform (a) and the top view of the platform (b), which shows the similarity with the double-body aircraft.

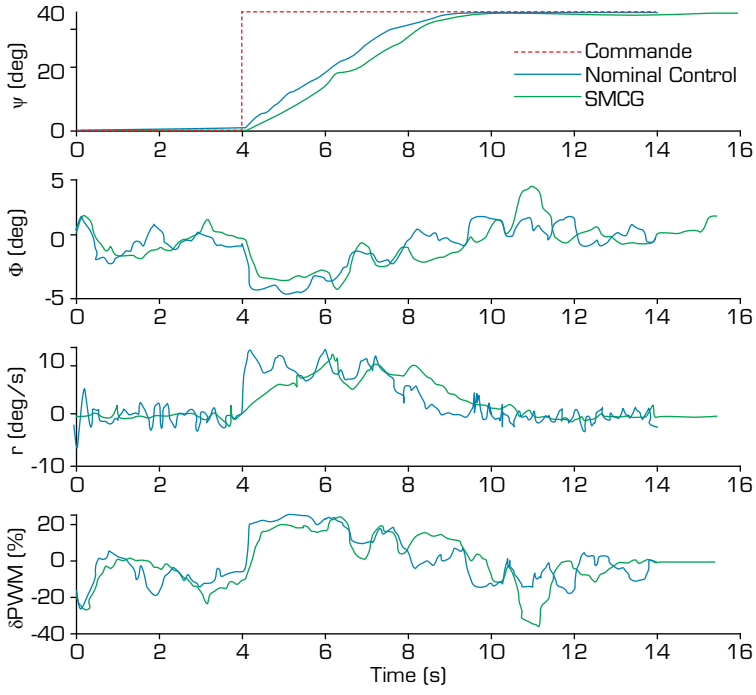

Source: Elaborated by the authors.

Figure 11. Experimental test results of nominal control system (blue lines) and bound control system (green lines) of SMCG.

CONCLUSION

The current research aimed to design a double-body aircraft flight control system with nominal and SMCG control laws. First, the modeling of a single and then a double-body aircraft was completed. The stability analysis of the single and double-body aircraft was investigated using a non-linear model and linearization was performed at a trim point. The eigenvalues were obtained, and the open-loop analysis showed that the double-body aircraft has seven dynamic modes. By identifying the behavior of the modes, it was found that the longitudinal channel modes have few changes, and the major changes are in the lateral-directional modes compared to the single aircraft, consistent with the literature. Two new modes have also been added in the lateral-directional channel, which are named relative roll I mode and relative roll II. Next, the flight control system was examined from a systemic perspective, and the centralized control system was introduced. It was shown that the centralized control system has lower costs and better performance than the distributed control system. The SMCG constraint control law was designed and numerical simulation showed that the designed SMCG constraint control law could follow the control commands with good precision and prevent the deviation of the angle of attack and yaw rate from the safety limits. This is due to the automatic reduction of the closed-loop system bandwidth. The deflection angles of the control surfaces and thrust commands were limited and reasonable, allowing common servos and motors the ability to follow them. The SMCG experimental implementation results showed that the add-on system's performance was also favorable in the real system and it can be implemented on cheap and small processors. Future research could focus on implementing the control algorithm on actual aircraft and the multi-body aircraft with more bodies can be dealt with.

CONFLICT OF INTEREST

Nothing to declare.

AUTHORS'CONTRIBUTION

Conceptualization: Azizi A; **Methodology:** Azizi A; **Software:** Azizi A; **Validation:** Azizi A and Abbasi Y; **Formal analysis:** Azizi A and Abbasi Y; **Investigation:** Azizi A; **Resources:** Sadati SH; **Data curation:** Azizi A; **Writing - Original draft:** Azizi A and Abbasi Y; **Writing - Review & editing:** Azizi A, Abbasi Y, and Sadati SH; **Final aproval:** Azizi A.

DATA AVAILABILITY STATEMENT

The data will be available upon request.

FUNDING

Not applicable.

ACKNOWLEDGMENTS

Not applicable.

REFERENCES

Ardalan V, Kolmanovsky I, Stefanopoulou A (2006) Constraint handling in a fuel cell system: a fast reference governor approach. IEEE Trans Control Syst Technol 15(1): 86-98. https://doi.org/10.1109/TCST.2006.883242

Babaei A-R, Hossein M (2021) Aircraft three-dimensional hardconstrained trajectory planning using pseudospectral optimization method. J Aerosp Technol Manag 13:e3521. https://doi.org/10.1590/jatm.v13.1170

Behrens A, Grund T, Ebert C, Luckner R, Weiss J (2020) Investigation of the aerodynamic interaction between two wings in a parallel flight with close lateral proximity. CEAS Aeronaut J 11(2):553-563. https://doi.org/10.1007/s13272-019-00435-9

Chao A, Changchuan X, Yang M, Chao Y (2019) Flight mechanical analysis and test of unmanned multi-body aircraft. International Forum on aeroelasticity and structural dynamics. Georgia, USA.

Cobar M, Montalvo C (2021) Takeoff and landing of a wing-tip-connected meta aircraft with feedback control. J Aircr 58(4):733-742. https://doi.org/10.2514/1.C035787

Cooper JR, Rothhaar PM (2018) Dynamics and control of in-flight wing tip docking. J Guid Control Dyn 41(11):2327-2337. https://doi.org/10.2514/1.G003383

Elmer G, Kolmanovsky I (1999) Fast reference governors for systems with state and control constraints and disturbance inputs. Int J Robust Nonlinear Control 9(15):1117-1141. https://web.eecs.umich.edu/~grizzle/GilbertFest/Gilbert(85).pdf

Köthe A, Behrens A, Hamann A, Nagel P, Nowka D, Lucker R (2017) Closed-loop flight-tests with an unmanned experimental multi-body aircraft. 17th International Forum on Aeroelasticity and Structural Dynamics. CEAS; Como, Italy.

Köthe A, Luckner R (2017) Flight path control for a multi-body HALE aircraft. In: Dołęga B, Głębocki R, Kordos D, Żugaj M, editors) Advances in aerospace guidance, navigation and control. Cham: Springer. p. 421-441.https://doi.org/10.1007/978-3-319-65283-2_23

Lars S, Chu QP, Mulder JA (2007) Nonlinear flight control design using constrained adaptive backstepping. J Guid Control Dyn 30(2):322-336. https://doi.org/10.2514/1.25834

Magill SA (2012) Compound aircraft transport study: wingtip-docking compared to formation flight (doctoral dissertation). Blacksburg: Virginia Polytechnic Institute and State University.

Meng Y, An Chao, Xie C (2022) Conceptual design and flight test of two wingtip-docked multi-body aircraft. Chinese J Aeronaut 35(12):144-155. https://doi.org/10.1016/j.cja.2022.01.020

Montalvo C, Mark C (2015) Meta aircraft flight dynamics. J Aircr 52(1):107-115. https://doi.org/10.2514/1.C032634

Mouhyemen K, Zafar M, Chatterjee A (2020) Barrier functions in cascaded controller: safe quadrotor control. 2020 American Control Conference. IEEE; Denver, USA. https://doi.org/10.23919/ACC45564.2020.9147864

Prado IAA, Santos DA (2017) A model predictive guidance strategy for a multirotor aerial vehicle. J Aerosp Technol Manag 9:116-128. https://doi.org/10.5028/jatm.v9i1.613

Troub B, Montalvo CJ (2016) Meta aircraft controllability. AIAA Atmospheric Flight Mechanics Conference 2016; Washington, D.C. https://doi.org/10.2514/6.2016-3395

Wei J, Li H, Guo M, Li J, Huan H (2021) Backstepping control based on constrained command filter for hypersonic flight vehicles with AOA and actuator constraints. J Aerosp Eng e8620873. https://doi.org/10.1155/2021/8620873

Wu M, Shi Z, Xiao T, Ang H (2019) Energy optimization and investigation for Z-shaped sun-tracking morphing-wing solar-powered UAV. Aerosp Sci Technol 91:1-11. https://doi.org/10.1016/j.ast.2019.05.013

Xu B, Sreenath K (2018) Safe teleoperation of dynamic UAVs through control barrier functions. IEEE International Conference on Robotics and Automation, 2018, pp 7848-7855, Brisbane, Australia. https://api.semanticscholar.orgCorpusID:52282925

Zhou H, Zheng Z, Guan Z, Ma Y (2020) Control barrier function based nonlinear controller for automatic carrier landing. 16th International Conference on Control, Automation, Robotics and Vision. IEEE; Shenzhen, China. https://doi.org/10.1109/ICARCV50220.2020.9305317

Zhu E, Zhou Z, Li H (2023) Modal analysis and flight validation of compound multi-body aircraft. Aerospace, 10(5):442. https://doi.org/10.3390/aerospace10050442

Zipfel PH (2000) Modeling and simulation of aerospace vehicle dynamics. Reston: AIAA.